Fundamental Electron-Precursor-Solid Interactions Derived from Time-Dependent Electron-Beam-Induced Deposition Simulations and Experiments

Jason D. Fowlkes[†],* and Philip D. Rack[†,‡]

[†]Nanofabrication Research Laboratory, Center for Nanophase Materials Sciences, Oak Ridge National Laboratory, Oak Ridge, Tennessee 37381-6487 and [‡]Materials Science and Engineering Department, The University of Tennessee, Knoxville, Tennessee 37996-2200

Nanoscale direct-write assembly methods, such as focused particle beam processing, require precise understanding and control of the relevant electron-precursor−solid interactions where energy beams on the order of 1−10 nm dictate the assembly/removal of material at the confluence of the particle beam, adsorbed precursor, and solid. Controlled assembly at this scale is critical as material defects are less tolerable at reduced sizes, which can compromise function. Materials and interfacial parameters that govern the flow of precursor to the growth area must be known in order to realize resolution limits and functional nanoscale properties. The major accomplishment of this work is the determination of the essential parameters that describe the electron-precursor−solid interactions that take place during the electron-beam-induced deposition (EBID) of nanoscale features and elements.

Electron-beam-induced processing (EBIP) is a direct-write technique well-suited for the deposition and/or etching of nanoscale features.[1−3] Recently, 3 nm spatial resolution[4,5] has been demonstrated, resolution limiting factors have been revealed,[6] and the statistics of ~1 nm resolution features have been quantified.[7] Mechanistically, EBIP occurs as a focused nanoscale beam of electrons dissociates adsorbed precursor molecules, either stimulating the localized deposition or etching of material depending on the chemical composition of the precursor molecule and substrate. Precursor molecules are delivered to the electron probe−substrate confluence, referred

ABSTRACT Unknown parameters critical to understanding the electron-precursor-substrate interactions during electron-beam-induced deposition (EBID) have long limited our ability to fully control this nanoscale, directed assembly method. We report here values that describe the precursor-solid interaction, the precursor surface diffusion coefficient (D), the precursor sticking probability (δ), and the mean precursor surface residence time (τ), which are critical parameters for understanding the assembly of EBID deposits. Values of $D = 6.4 \ \mu m^2 \ s^{-1}$, $\delta = 0.0250$, and $\tau = 3.20$ ms were determined for a commonly used precursor molecule, tungsten hexacarbonyl $W(CO)_6$. Space and time predictions of the adsorbed precursor coverage were solved by an explicit finite differencing numerical scheme. Evolving nanopillar surface morphology was derived from simulations considering electron-induced dissociation as the critical depletion term. This made it possible to infer the space- and time-dependent precursor coverage both on and around nanopillar structures to better understand local precursor dynamics during mass-transport-limited (MTL) and reaction-rate-limited (RRL) EBID.

KEYWORDS: electron-beam-induced deposition · nanofabrication · EBID · directed assembly

to here as the beam interaction region (BIR), by a capillary needle to facilitate enhanced growth/etch rates.

Many recent experimental studies related to EBID have focused on understanding fundamental parameters that affect the dynamic nanopillar growth process. These studies have addressed challenges specific to EBIP, including understanding deposit chemistry,[8] physical broadening,[4] etch chemistries,[9,10] thermal,[11] pressure,[12,13] and accelerating voltage[14] effects.

The fundamental parameters that govern EBIP have also been thoroughly explored *via* simulations.[15−20] Efforts aimed at understanding the electron−solid, electron−precursor, and precursor−solid interactions[1,10,11,15−17,21−24] have been especially useful for interpreting the experimental results reported in this work. Here we report estimates of the parameters that characterize the precursor−solid interaction, including the precursor surface

diffusion coefficient (D), mean precursor surface residence time (τ), and precursor sticking probability from the vapor (δ) for the EBID deposition of W-based deposits from the $W(CO)_6$ precursor on a silicon wafer substrate. Pulsing of the electron beam was crucial for this study by making it possible to explore a wide range of EBID parameter space. For example, Plank *et al.* have demonstrated the inverse relationship arising between electron probe dwell time (τ_d) and volumetric growth efficiency (γ, atoms deposited per electron) for the MTL pulsed EBID of platinum using the $C_9H_{16}Pt$ precursor.[25] In addition to demonstrating a steep rise in γ with reduced beam dwell time at constant precursor refresh time (τ_r), Plank *et al.* also demonstrated an improvement in γ by increasing the primary electron probe size *during spot dwell mode*.[25] Beam defocus effectively mitigates the extreme MTL condition in the BIR by reducing the current density there. Reduced precursor dissociation is concomitant with the drop in current density at the apex. Thus, by implementing a beam defocus, Plank *et al.* showed that γ can be increased as surface diffusion redistributes precursor over the nanopillar in a more efficient spatial profile for dissociation; γ goes up as an increase in lateral growth overcompensates for the reduction in vertical growth rate.[25] This proposed model of volumetric evolution during EBID was shown to be in agreement with our Monte Carlo based predictions reported in ref 17 under similar MTL conditions.

Here, an array of experimental data was generated starting from the MTL growth condition where deposition efficiency is poor and vertical growth rates are slow; precursor surface coverage (θ) decreases well below the equilibrium value (θ_o) for sustained periods. RRL EBID ensues when θ in the BIR remains at or near θ_o during EBID. The RRL growth condition was achieved by beam pulsing for enhanced precursor refresh to compensate for a low precursor flux. The maximum atom per electron efficiency achieved using RRL EBID was used to estimate the mean electron stimulated dissociation cross section $\bar{\sigma}_{30keV}$ for the $W(CO)_6$ precursor. The electron-stimulated dissociation cross section of the adsorbed precursor molecule governs dissociation and deposition (see Supporting Information S1).[17,18] Three unknown variables remained (D, τ, δ) once reasonable approximations of $\bar{\sigma}_{30keV}$, the local precursor flux (Φ_{gas}),[12,13,26] and the electron flux[15,17,18,24] at the substrate surface were determined. Convergence by a least-squares process was used to fit simulated results to the time-dependent experimental data in order to determine the best fit parameter set from a large array of initial guesses. Results are compared and contrasted with published data[27−30] reporting nanopillar features grown using the $W(CO)_6$ precursor molecule (see Supporting Information S2). Our results also agree with predictions from Utke's scaling law analysis of steady-state precursor coverage during EBID.[19]

RESULTS

Precursor gas is supplied to the beam interaction region directly from the vapor phase as well as by the surface diffusion of adsorbed precursor gas. Figure 1a illustrates several potential pathways for gas to arrive at the BIR. The relative contributions of these precursor flux pathways to the BIR dictate the vertical growth rate, final nanopillar morphology, and resolution under mass-transport-limited conditions. Figure 1b−d illustrates pulsed beam irradiation for two example loop cycles, as shown in blue where on/off represents the beam blanking status and the red traces illustrate precursor surface coverage (see Supporting Information S3). The total EBID growth time, $t_g = N\tau_d$, is a measure of electron dose, and N is the total number of loops. Recurring loop numbers are referred to using the lower case variable (n).

MTL growth was observed for EBID conducted using the constant (nonpulsed) beam irradiation mode. Figure 1e shows final nanopillar height (h_f) *versus* electron dose, which demonstrates a sublinear increase in nanopillar height with growth time, indicating MTL growth; the instantaneous vertical growth rate (iVGR $= dh/dt_g$) steadily decreases with increasing electron dose.

MTL growth is also evident in the results shown in Figure 2a, where final nanopillar height *versus* τ_r is displayed (red data points). The data demonstrate a significant increase in nanopillar height as a function of increasing refresh time for a constant dose (the final height is increasing at a fixed total growth time as τ_r is increased).

The superimposed black line in Figure 2a represents the best fit of simulation results to the refresh set of experiments, determined using least-squares (eq 9) curve fitting to determine the most converged solution. The best fit solution ($D = 6.4\ \mu m^2\ s^{-1}$, $\tau = 3.20$ ms, and $\delta = 0.0250$) fell within experimental error for each of the seven experiments. These parameters yield a predicted equilibrium precursor surface coverage of $\theta_o = 0.256$. Simulation results presented in the remaining figures all used this parameter set and are indicated with hatched lines. Additional simulation solutions to the refresh set are also shown in Figure 2a that bound the error bars along their maximum and minimum extents as a measure of error (light gray curves) for the *coupled* (D,τ,δ) parameter set (see Supporting Information S4).

The vertical growth rate (VGR) was further improved by decreasing τ_d at the optimized refresh time of 8 ms, where the VGR is the final nanopillar height divided by the total growth time (h_f/t_g). Figure 2b shows the observed increase in the nanopillar height as a function of decreasing τ_d from 1 to 0.125 ms at constant dose ($t_g = 2.5$ s) (see Supporting Information S5). Figure 1c schematically illustrates the increase in precursor surface coverage, per loop ($\tau_d + \tau_r$), achieved by reducing τ_d at constant τ_r relative to Figure 1b. The VGR increased with
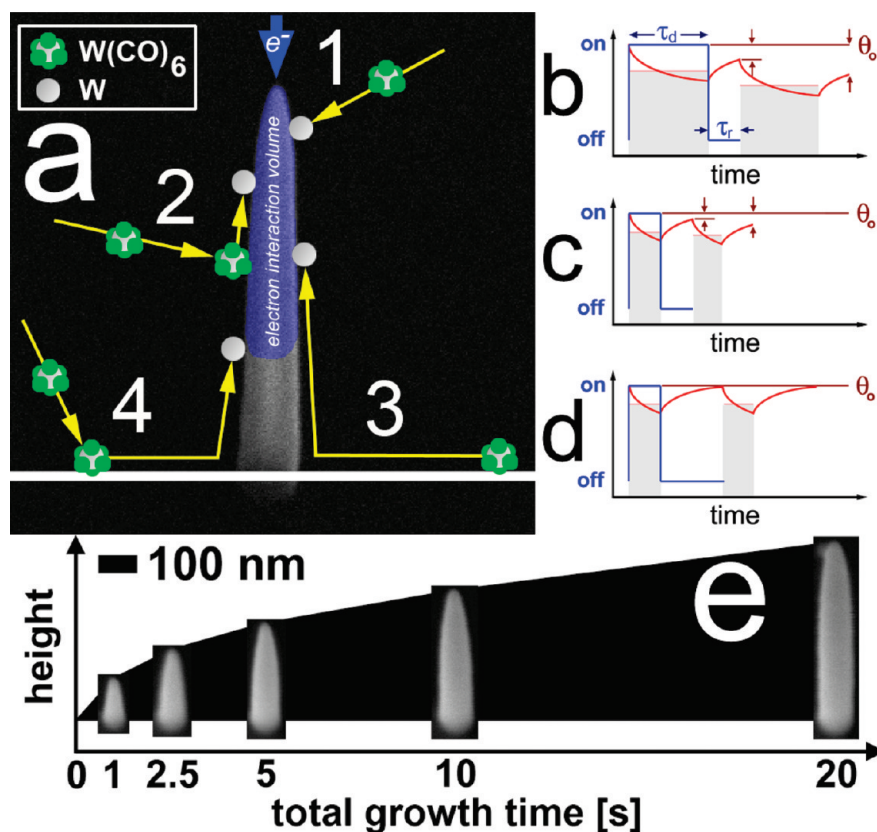
Figure 1. (a) SEM image-schematic overlay that demonstrates the different mechanisms by which precursor gas may arrive at the nanopillar apex and can contribute to electron-beam-induced precursor dissociation. **(b−d)** Schematic illustrations of precursor coverage (θ, red) at various dwell (τ_d) and refresh times (τ_r) for mass-transport-limited (MTL) growth. Two loop cycles are shown for each example. Equilibrium coverage (θ_o) is indicated by the dark red line. The superimposed shaded bar indicates the average precursor coverage during each dwell increment. The digital blue line represents the blanking status of the electron probe in spot mode. **(e)** MTL EBID in spot dwell mode with no refresh cycle and localized precursor flow on. The rate of increase of nanopillar height was observed to decrease as a function of increasing total growth time (t_g). The beam accelerating voltage was 30 keV, and the beam current was 79 pA. The SEM images were acquired at 30° beam incidence.

decreasing τ_d due an increase in adsorbed precursor coverage on the nanopillar surface. Simulation results are shown as the superimposed, hatched black line in Figure 2b. The simulation predicted the increase in final nanopillar height with decreasing beam dwell time and also predicted the observed saturation in h_f for EBID experiments conducted at $\tau_d = 125-250$ μs. The VGR was very nearly maximized by pulsed EBID at the $i_b = 73$ pA, $\tau_d = 125$ μs, and $\tau_r = 8$ ms growth condition, indicating a recipe approaching RRL conditions.

RRL conditions were ultimately achieved experimentally by reducing i_b from 79 to 25 pA at the optimized pulse settings of $\tau_d = 125$ μs and $\tau_r = 8$ ms. Moreover, it was found that, by reducing the current to 25 pA, the beam dwell time could be increased from 125 μs up to 1 ms with RRL conditions conserved as further reductions in either the current or dwell time did not increase the VGR. Figure 2c shows the evolution of nanopillar height as a function of increasing the electron dose for the RRL condition $i_b = 25$ pA, $\tau_d = 1$ ms, and $\tau_r = 8$ ms (blue data points). The benefit in the current reduction can be seen in the figure where the iVGR (slope) for the

$i_b = 73$ pA, $\tau_d = 125$ μs, and $\tau_r = 8$ ms condition (green data points) is 20% lower than for the RRL condition (blue data points). For comparison purposes, an additional EBID growth MTL mode is provided (red data points), where the simulation showed excellent agreement with experimental results (black, hatched line).

Figure 2d presents the vertical (ε) and volume growth efficiencies for several EBID conditions where ε is the length of nanopillar deposited per electron. As mentioned previously, condition 4 (25 pA, $\tau_d = 1$ ms, $\tau_r = 8$ ms) represents RRL EBID while condition 1 exhibited MTL EBID, and conditions 2 and 3 exhibited "mixed regime"[20] behavior (defined below). The volumetric growth efficiency reached a maximum value of 0.08 atoms per electron.

On the basis of earlier reports, RRL growth conditions were expected to yield an atom per electron efficiency of $\gamma \sim 8 \times 10^{-3}$ based on the dissociation cross section of $W(CO)_6$. This range is an estimate based on the expression $\bar{\sigma}_{30keV} \times \theta_o \times s_p$, where $\bar{\sigma}_{30keV}$ is the reported dissociation cross section for $W(CO)_6$ at 30 keV (1.2×10^{-2} nm²)[30] and $s_p = 0.63$ $W(CO)_6$ molecules
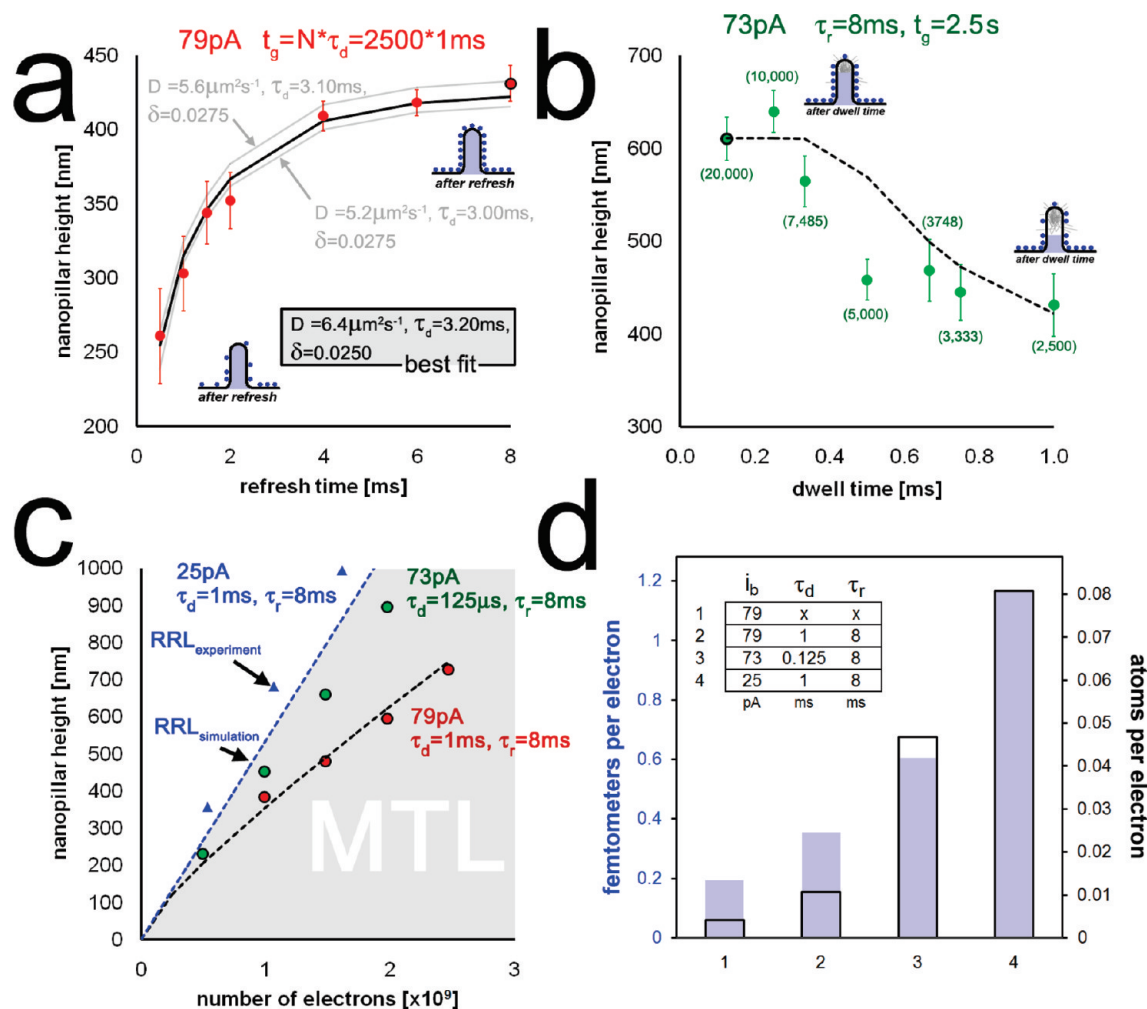
Figure 2. (a) Final nanopillar height as a function of increasing gas refresh time (red dots). The total growth time (t_g = 2.5s) was constant for each data point as well as the beam accelerating voltage (E_o = 30 keV) and the sample current (i_b = 79 pA). Each nanopillar was grown in spot mode but blanked (*i.e.*, looped) in 2500 consecutive steps with a probe dwell time of τ_d = 1 ms. The best fit simulated data (solid black line) yielded the following precursor parameters: D = 6.4 μm^2 s^{-1}, τ = 3.20 ms, and δ = 0.0250 for W(CO)$_6$. Two additional solutions (light gray lines) are shown that best trace the upper and lower extremities of the experimental error bars. (b) W-based nanopillars grown at 30 keV, 79 pA, with a total growth time t_g = 2.5 s. This data set explored the effect of a reduction in dwell time (τ_d), while maintaining a constant total dose t_g = $N\tau_d$ = 2.5 s (green dots). The refresh time was fixed at τ_r = 8 ms for each experiment. The number of loops for each experiment is shown in green brackets to maintain a constant dose. The simulated curve is shown as the hatched black line, where the fitted precursor parameters from panel a were used. (c) Nanopillar height *vs* total growth time (t_g), where the growth time coordinate has been converted to total number of electrons. The beam current (i_b) and the pixel dwell time (τ_d) are labeled for each curve in the figure; E_o = 30 keV and τ_r = 8 ms for all experiments shown. The experimental RRL EBID was achieved at the 25pA beam current setting (blue triangles). The simulated RRL line is shown as the hatched blue line superimposed over the figure. An additional simulation/experiment pair is shown for a select MTL condition again exemplifying an excellent fit (red dots). (d) Vertical (ε, fm per electron, blue shaded bar plot) and volumetric growth efficiencies (γ, atoms per electron, black outline) for select EBID experiments.

nm^{-2}. The maximum deposition efficiency achieved in this work was γ = 0.08 atoms per e$^-$ (ε = 1.2 fm per e$^-$), yielding a $\bar{\sigma}_{30keV}$ = $\gamma/(s_\rho \times \theta_o)$ = 0.50 nm^2, approximately 42-fold higher than the value reported in the literature.[30] In Supporting Information S6, we suggest that perhaps MTL conditions led to the underestimation of $\bar{\sigma}_{30keV}$ reported in the literature.[30]

DISCUSSION

Figure 3 shows a series of simulated precursor surface coverage plots at the nanopillar apex $\theta(r = 0,t)$ for select EBID simulations to demonstrate the precursor coverage changes that take place during pulsed EBID.

Figure 3a shows that (see Supporting Information S7 for a detailed description of how to interpret the form of data display in Figure 3) apex coverage not only varies on a per loop basis ($\tau_d + \tau_r$) but also steadily decreases over the course of multiple EBID loops. The steady decay of $\theta(r = 0,t)$ approaches a steady-state value of ~0.062, or 30% of θ_o, near the end of the growth. This is demonstrated by the 3D profiles of precursor coverage in Figure 3a, showing significant precursor depletion at the apex (see Supporting Information S8).

MTL EBID conditions prevailed for the long dwell (τ_d = 1 ms) and short refresh (τ_r = 0.5−2 ms) experi-
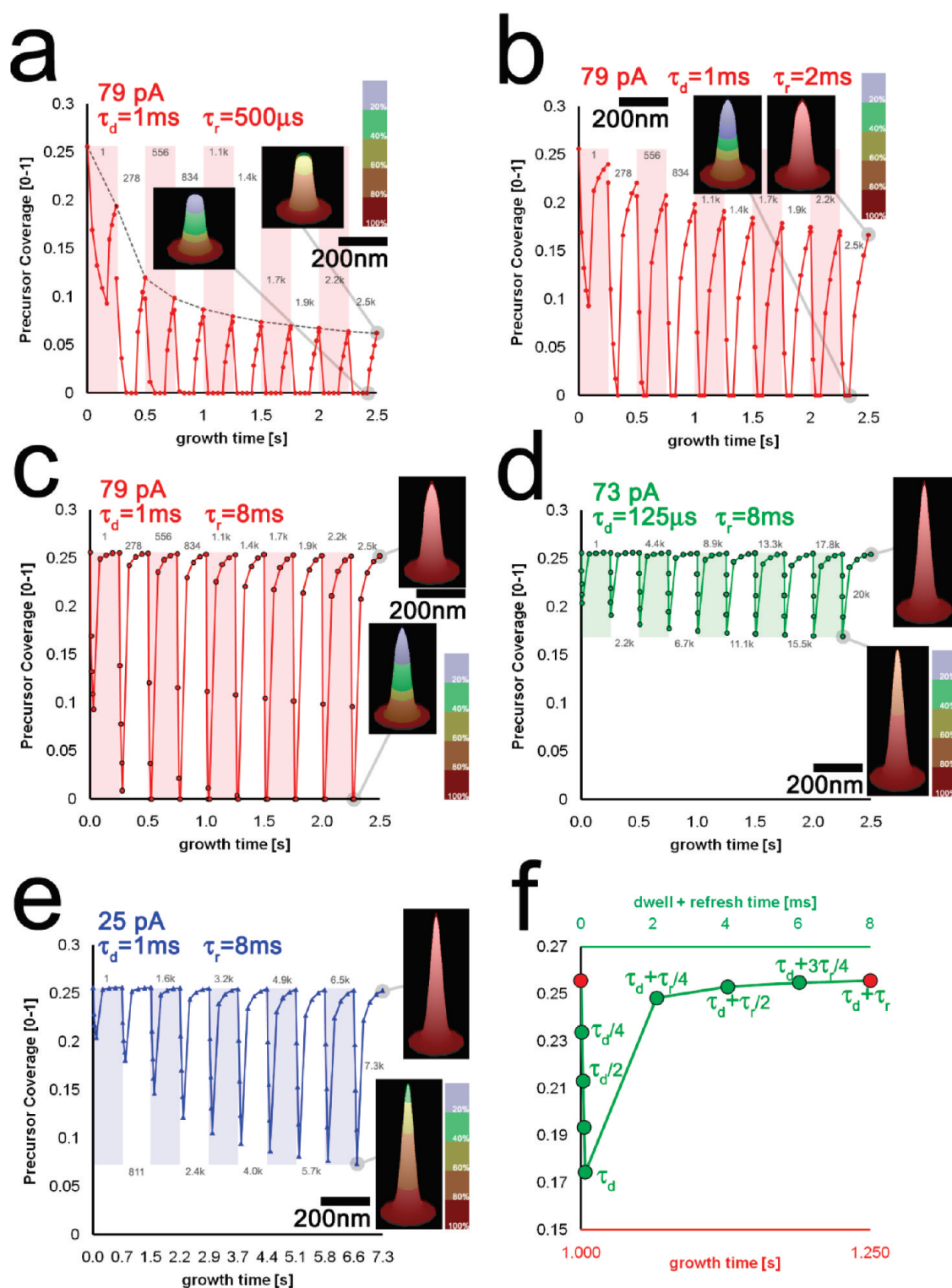
Figure 3. Simulated results for the precursor coverage (θ) at the nanopillar apex as a function of total growth time (t_g) for select virtual EBID experiments. (a−e) Coverage was sampled every N/10 loops (where N is the total number of loops). The loop number is shown superimposed over each figure (in gray), and alternating shading indicates the change in loop number. The coverage during ×5 dwell (τ_d) and ×5 refresh (τ_r) increments are shown for each loop. It is important to note that the time coordinate (x-axis) only corresponds to data points at boundaries between loops. (f) Best illustrates this concept where the data points for an example growth loop are shown. The red data points located at the loop boundary are referenced to the axis shown in red, which is on the scale of seconds. The remaining data points are referenced to $\tau_d + \tau_r$ time, as shown, which in on the order of milliseconds.

ments conducted at 79 pA. Increasing τ_r from 0.5 to 2 ms significantly improves the fraction of precursor re-

freshed to the apex per loop (compare Figure 3a,b). Simulations show that a refresh time of 8 ms is required

to fully replenish the BIR to $\theta_o = 0.256$ when using a beam dwell time of 1 ms (Figure 3c). We call this mixed mode EBID, consistent with Rykaczewski et al., as they previously identified this regime in their investigations of EBID under high vacuum, spot dwell conditions where diffusion conditions dominate.[20] In the mixed mode, precursor coverage decreases during the electron beam dwell, but fully recovers to θ_o after the refresh period because τ_r is sufficiently long. In contrast, under the MTL conditions (Figure 3a,b), the coverage at the apex, following refresh, continuously decreases over the total growth time. Mixed mode conditions arise on initially short nanopillar structures due to the significant reservoir of adsorbed precursor located beneath the BIR (inset Figure 3c), coupled with the impinging precursor flux, which effectively acts to minimize the diffusion distance.

Precursor surface diffusion, the effective precursor impingement rate ($\delta \times \Phi_{gas}$), and the mean precursor residence time all contribute to the replenishment of precursor at the apex during the dwell and refresh periods. In order to approximate the individual contributions of the vapor flux and surface diffusion flux to the apex precursor concentration, decoupled control simulations were executed using the best fit solution set. Specifically, simulations were repeated for the variable refresh data set (Figure 2a) to compare the separate contributions of vapor flux and surface diffusion to EBID. The details are described in Supporting Information S9.

The results presented in Figure 4 suggest that direct precursor impingement at the BIR (Figure 1a, case 1) dominates precursor refresh at the apex during MTL EBID (Figure 3a,b) (see Supporting Information S10). In contrast, during mixed mode EBID (Figure 3c,d), the iVGR depends on the interplay between all of the precursor refresh mechanisms illustrated in Figure 1a. Rykaczewski et al. have shown that during mixed mode EBID the diffusion time scale and mass sink (reaction) time scale, respectively, are within an order of magnitude ($t_{diff} \approx t_{sink}$).[20] In addition, the observation time scale (t_{obs}) is $t_{obs} \gg t_{diff}$ and t_{sink}, leading to the steady-state condition between diffusion and reaction of[20]

$$\frac{t_{sink}}{t_{diff}} \frac{1}{r^*} \frac{\partial}{\partial s^*}\left(r^* \frac{\partial C^*}{\partial s^*}\right) - C^* \dot{Q}_s^* = 0 \qquad (1)$$

$$\left.\frac{\partial C^*}{\partial s^*}\right|_{s=0} = 0 \qquad (2)$$

$$C^*|_{s \to \infty} = C_\infty^* \qquad (3)$$

where $*$ indicates non-dimensional form, s is a single curve linear coordinate (arc length), $\dot{Q}_s^*$ is the reaction term describing the precursor dissociation term, and C^* is the surface precursor concentration.[20] These equations describe the diffusive transport for our system when the precursor coverage at the nanopillar reaches
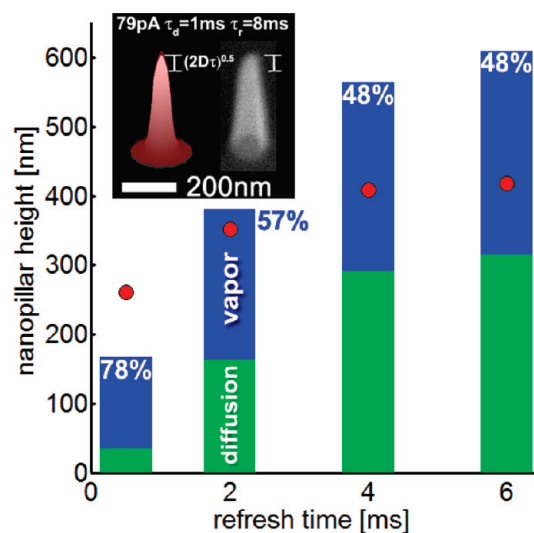

Figure 4. Stacked bar plot showing the total nanopillar height predicted by two independent EBID simulations; (blue) estimating the fraction of final nanopillar height considering precursor refresh only by direct vapor refresh and (green) estimating the fraction of final nanopillar height considering precursor refresh by adsorbed surface diffusion. Experimental results are shown in red (duplicated from Figure 2a). (Inset) Experimental and simulated nanopillar for the i_b = 79 pA, τ_d = 1 ms, and τ_r = 8 ms EBID growth mode. Simulations were conducted where gas flux (Φ_{gas}) was inhibited for pixels located within a distance of $0.5 \times$ MSD from the nanopillar apex where MSD = $(2D\tau)^{0.5}$ = 202 nm and is the mean square displacement of the $W(CO)_6$ precursor molecule on the nanopillar surface (see Figure 4 inset). This effectively silences the contribution of vapor flux to the EBID growth but maintains the appropriate surface coverage outside the BIR to support diffusive transport. A second set of simulations was conducted with $D = 0$ μm^2 s^{-1} to determine the contribution of direct precursor impingement at the apex ($\delta \times \Phi_{gas}$) to EBID.

equilibrium (compare with eq 6). For example, the time-coverage traces in Figure 3c−e indicate near steady-state conditions at N for these experiments, where $t_{obs} \sim 10^0$ s, $t_{diff} \sim 10^{-3}$ s, and $t_{sink} \sim 10^{-2}-10^{-3}$ s. Significant precursor coverage on the nanopillar surface, even under MTL conditions, suggests that the parameter set (D,τ,δ) represents predominantly the precursor−nanopillar interaction as opposed to the precursor−substrate (Si) interaction. Thus, precursor dissociation and the subsequent deposition arise mostly from precursor that adsorbed, or absorbed and then diffused, on the nanopillar surface.

Figure 3e shows $\theta(r = 0,t)$ for the simulated RRL condition. By lowering i_b to 25 from 79 pA, at τ_d = 1 ms and τ_r = 8 ms, the maximum VGR was achieved experimentally. Simulation results show that a lower current per beam dwell period (1) consumes fewer precursor molecules on the nanopillar side walls, (2) allows more molecules to diffuse to the nanopillar apex during the dwell, and (3) consumes fewer molecules per unit dwell, all leading to a higher VGR. For these same reasons, Plank et al. observed an increase in volumetric growth efficiency under spot dwell (nonpulsed) conditions by reducing the effective current density in the BIR defo-

TABLE 1. Analytical, Experimental, and Simulated Results for Electron-Beam-Induced Deposition under Steady-State Growth Conditions[a]

i_b	τ	P	δ	D	θ_o	$\Phi_{electrons}$	Φ_{gas}	σ	$FWHM_B$	$(D\tau)^{1/2}$	$\tilde{\tau}$	$\tilde{\varphi}$	$\tilde{\rho}$	$\tilde{\varphi}$	$\tilde{\varphi}$
pA	ms	mPa		$\mu m^2 s^{-1}$		$nm^{-2}s^{-1}$	$nm^{-2}s^{-1}$	nm^2	nm	nm	analyt			sim	exp
79	3.2	333.3	0.025	6.4	0.256	2.5E+05	2.7E+03	0.50	35.3	143.1	301.5	2.87	0.06	2.68	2.7
25	3.2	333.3	0.025	6.4	0.256	8.0E+04	2.7E+03	0.50	35.3	143.1	95.3	2.57	0.10	2.03	2.4

[a]Predictions of diffusive replenishment $\tilde{\rho}$,[19] normalized deposit size $\tilde{\varphi}$,[19] and precursor depletion at the nanopillar apex $\tilde{\tau}$[19] calculated for steady-state EBID at 25 and 79 pA settings using the best fit parameter set (D = 6.4 $\mu m^2 s^{-1}$, τ = 3.20 ms, δ = 0.0250) and the additional conditions listed in the table; $\tilde{\varphi}$ can also be calculated directly from nanopillar physical dimensions using eq 4 (last column). Thus, $\tilde{\varphi}$ was derived from time-dependent simulations of EBID (shaded in red) as well as from EBID experiments (last column). Care was taken to execute the simulation until steady-state growth conditions were achieved (t_g = 2 s for 25 pA simulations and t_g = 4 s was required for 79 pA simulations) in order to accurately compare simulation results with the predicted value of $\tilde{\varphi}$ in eq 5.

cusing the beam.[25] In both our work and ref 25, the effective current density in the BIR was reduced. However, in the results reported here, this reduction was accomplished by reducing the current at fixed beam size ($\Delta i_b/A$), while Plank *et al.* increased the beam diameter at fixed current ($i_b/\Delta A$).[25] Thus, beam defocus leads to an improvement in lateral (and volumetric) growth efficiency in nonpulsed mode,[25] while reducing the current in pulsed mode leads to an improvement in vertical growth efficiency.

Further reductions in either i_b (at constant τ_d) or τ_d (at constant i_b) produced negligible changes in VGR. Therefore, the i_b = 25 pA, τ_d = 1 ms, and τ_r = 8 ms condition was deemed the RRL condition. Figure 2c shows just how closely the simulated RRL condition (hatched, blue line) reflected the RRL experiments (blue date points), where the plot shows nanopillar vertical growth rate *versus* dose.

Surprisingly, large precursor depletion occurs during the dwell time at the nanopillar apex (Figure 3e) for simulations mimicking the RRL condition. How could such a high efficiency coexist with significant precursor depletion at the apex? It was striking to find, for example, that coverage dropped to $0.27 \times \theta_o$ after only $\tau_d/4$ of the dwell period at the n = 5000 loop. A low electron flux at the apex was determined to cause this apparent discrepancy when the ratio of SEs emitted per adsorption site per dwell period was considered. Calculations revealed that, at most, one dissociation event per dwell is anticipated at 25 pA and depletion following dissociation is tolerable, without a drop in efficiency, for the short dwell period of 1 ms because the chance of a second dissociation event at any pixel is ~0, due to a low electron flux, regardless if a precursor molecule is adsorbed or not (see Supporting Information S11). This hypothesis was confirmed by executing a simulation under the same conditions (i_b = 25 pA, τ_d = 1 ms, t_g = 7.3 s) but artificially fixing the precursor coverage to θ_o = 0.256 during the simulation, regardless of the precursor dissociation rate. Thus, this simulation yields the maximum possible vertical growth rate (for the θ_o = 0.256 coverage condition). The final nanopillar height was found to equal the result obtained from the gas dynamics simulation (see the precursor trace in Figure 3e that shows the significant depletion of precursor during the dwell period), indicating that the RRL condition had been reached.

The precursor coverage profiles displayed in Figure 3d,e seem contradictory with the growth efficiencies determined for each of these conditions. For example, the average precursor coverage per dwell cycle was actually higher for the 73 pA experiment (Figure 3d) yet had a lower VGR. Clearly, the VGR should scale in proportion with the magnitude of $\theta(r = 0,t)$. However, even though the mean precursor coverage during the total dwell period is lower for the 25 pA setting, the coverage at any instant within the dwell period is higher for the 25 pA case (this comparison must, and was, made at constant dose as shown in Supporting Information S12). The instantaneous precursor coverage per elapsed time during the dwell cycle is higher for the 25 pA, τ_d = 1 ms case, relative to the 73 pA, τ_d = 125 μs case, leading to the higher vertical growth efficiency.

The EBID growth regime and nanopillar morphology predictions made in this paper agree remarkably well with calculations reported for steady-state EBID growth.[19] In ref 19, scaling laws were derived relating nanopillar deposit lateral resolution to the critical variables (Φ_{gas}, D, δ, τ, *etc.*) that limit precursor coverage during EBID. Table 1 presents the calculations for several dimensionless ratios reported in that work describing diffusive replenishment $\tilde{\rho}$, normalized deposit size $\tilde{\varphi}$, and precursor depletion at the nanopillar apex $\tilde{\tau}$ during steady-state EBID. Calculations were made for steady-state EBID conducted at 25 and 79 pA with no refresh ($\tau_d = t_g$ and $\tau_r = 0$) using the best fit parameter set. Simulations were also executed under these conditions until steady-state nanopillar growth was reached in order to compare our simulated results with predictions from Utke's equations. Superimposing our results on a parameter space map (Figure 5) relating $\tilde{\varphi}$ *versus* $\tilde{\rho}$ (reproduced from Figure 3[19]), we found that both predictions (●) and calculations (+) fall within the MTL regime, in proximity to the diffusion-enhanced approach to RRL conditions. By implementing a refresh cycle, we
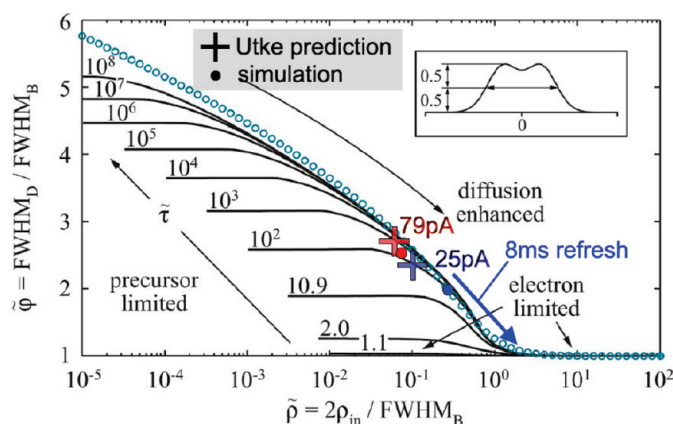
Figure 5. Normalized deposit lateral resolution *vs* normalized diffusive replenishment for various values of precursor depletion at the nanopillar apex. The superimposed crosses (25 pA, blue; 79 pA, red) emphasize two select data points from this work. Their location in the diagram suggests MTL conditions where the diffusion path to the nanopillar apex limits the vertical growth rate. However, close proximity to the RRL (electron limited) line indicates that a small increase in precursor refresh time would facilitate additional vertical nanopillar growth by diffusion to the apex which was, indeed, observed in the time-dependent simulations conducted in this work (Figure 3a−c and Figure 4). Reprinted with permission from ref 19. Copyright 2007 American Vacuum Society.

effectively moved down the diffusion-enhanced line to the RRL condition; Figure 4 shows the increasing contribution of diffusion to refresh at the apex (see Figure 3a−c and Figure 4) (see Supporting Information S13).

The dimensionless parameter describing the normalized deposit size was determined directly from our experimental and simulation results using[19]

$$\tilde{\varphi} = \frac{\text{fwhm}_{\text{deposit}}}{\text{fwhm}_{\text{beam}}} \qquad (4)$$

This result was then compared with a predicted value computed using

$$\tilde{\varphi} \approx \sqrt{\log_2\left(2 + \frac{\overline{\sigma}_{30\text{keV}}\Phi_e \tau s_\rho}{s_\rho + \delta\tau\Phi_{\text{gas}}}\right)} \qquad (5)$$

where Φ_e is the peak electron flux at the deposit apex.[19] These equations provided a very powerful means to compare experiments, predictions, and simulations. A predicted value for φ was determined by inserting the

best fit parameter set (D,τ,δ) into eq 5 and subsequently comparing these results with measurements of $\tilde{\varphi}$ from both experiment and simulation (Table 1). At the 79 pA setting, the predicted value of ($\tilde{\varphi} = 2.87$) matched our experimental ($\tilde{\varphi} = 2.7$) and simulated result ($\tilde{\varphi} = 2.68$) to within 6%. Such precise agreement in $\tilde{\varphi}$ indicates the convergence of methods between the scaling law based predictions of ref 19 and the time-dependent continuum simulation predictions reported here. In addition, the agreement between experimental and simulated measurements adds validation to the estimates for D, τ, and δ as reported. The simulation yielded a nanopillar aspect ratio of ($\tilde{\varphi} = 2.03$) for the 25 pA setting, which is smaller than predicted by initial calculation ($\tilde{\varphi} = 2.57$) and experiment ($\tilde{\varphi} = 2.4$). Yet, even this level of agreement between values is promising considering that $\tilde{\varphi}$ spans a potential range of 0−6. Thus, our simulated predictions seem to not only agree with real EBID experiments but also are in agreement with predictions reported by Utke.[19]

CONCLUSIONS

Determination of the parameter set ($D = 6.4 \ \mu\text{m}^2 \text{s}^{-1}$, $\delta = 0.0250$, $\tau = 3.20$ ms) for the precursor molecule $W(CO)_6$ used during EBID constitutes a significant step in our understanding of the electron−precursor−solid interactions. Our results suggest that the determined parameter set describes the precursor−deposit interaction because precursor replenishment and consumption were found to take place mostly on the growing deposit indicating that (D,δ,τ) can be substrate-independent for certain growth regimes. The simulated and fitted prediction (1) fell within experimental error for the fitted parameter set, (2) replicated a broad range of experimental data within experimental error, and (3) agreed well with published methods for predicting nanopillar morphology under steady-state growth conditions.[19] This contribution constitutes a significant advancement in directed nanoscale assembly by revealing quantitative parameters that must be known in order to control evolving physical dimensions during EBID direct-write synthesis.

METHODS

EBID Experiments. Tungsten-based nanopillars were deposited on Si(001) wafer substrates by the electron-stimulated dissociation of tungsten hexacarbonyl $W(CO)_6$ precursor gas at the wafer surface. The native oxide layer on the Si wafer substrate surface was not removed prior to nanopillar growth. The experiments described below were conducted on a FEI Nova 600 dual electron-ion beam system equipped with a localized gas injection nozzle diameter (500 μm) connected to a reservoir of the $W(CO)_6$ precursor (see Supporting Information S14). The $W(CO)_6$ precursor is a solid source that is heated to $T = 55$ °C for sublimation. The nozzle was angled at 50° with respect to the substrate surface and set to 100 μm from the surface as measured from the bottom of the nozzle to the substrate surface. The $W(CO)_6$ precursor vapor pressure at the beam interaction re-

gion was estimated to be 330 mPa by simulation. A simulator was written and compiled based on a combination of Utke and Wich's methods to arrive at this estimation.[12,13,26] Simulation performance was deemed representative of experimental conditions by regenerating Utke's precursor−substrate coverage profiles presented in the literature (see Supporting Information S15).[12,13]

EBID Experiments Were Conducted with and without Gas Flow. The gas flow was turned on prior to each experiment to establish the equilibrium precursor surface coverage (θ_o) as the initial condition; θ_o was determined by modulating the gas exposure time just prior to EBID. Then, θ_o was established once a change in precursor flow time had no observable affect on the final nanopillar morphology at constant dose; θ_o was established at $\Delta t > 5$ s of preflow (although our final results indicate that θ_o is estab-

lished in <1 s, and instrumentation effects account for the majority of the 5 s preflow time).

Precursor flow increased the background chamber pressure increased from 7.0×10^{-2} to 1.5 mPa. EBID experiments were also conducted with the gas flow off as a control in order to determine the contribution of residual chamber gas and hydrocarbons to the growth process.

EBID experiments were conducted using an electron accelerating beam voltage (E_o) of 30 keV. Nanopillar growth was conducted at two different beam current settings of 25 and 79 pA as determined by Faraday cup measurements. The 30 μm current limiting aperture was used for all experiments. The effective electron beam diameter predicted for each case was 11 nm (25 pA) and 17.8 nm (79 pA) as suggested by the tool specifications, yet we found these values to be 20 and 25 nm, respectively. Electron beam focus was quantified by sample current measurements acquired during EBID; maximizing the rate of change in sample current with time (di_s/dt) at short growth times represents the smallest probe focus.[21,31] Additional, critical experimental controls are discussed in Supporting Information S16. Control experiments were conducted to confirm a minimal contribution from residual hydrocarbon species present in the chamber to EBID (see Supporting Information S17).

EBID Finite Difference Simulation. The time-dependent parabolic diffusion equation describing the change in precursor surface concentration as a function of time $\partial C(r,s,t)/\partial t$ was solved using an explicit finite differencing numerical scheme considering the additional factors of precursor arrival rate, electron-induced precursor dissociation, and precursor adsorption/desorption integral to EBID

$$\frac{\partial C(r,s,t)}{\partial t} = \frac{D}{r}\left(\frac{\partial r}{\partial s}\frac{\partial C(r,s,t)}{\partial s} + r\frac{\partial^2 C(r,s,t)}{\partial s^2}\right) -$$
$$\bar{\sigma}_{30keV}\frac{\partial r}{\partial s}\frac{\delta_{SEI}\left(1 + \sec\left(\tan^{-1}\frac{\partial h(r,t)}{\partial r}\right)\right)i_b}{2\pi q w^2}e^{-r^2/2w^2}C(r,s,t) + \delta\Phi_{gas}$$
$$\left(1 - \frac{C(r,s,t)}{s_\rho}\right) - \frac{C(r,s,t)}{\tau} \quad (6)$$

where the radial form of the diffusion equation was used. The mathematical terms appearing on the right-hand side of eq 6, from left-to-right, describe precursor surface diffusion, precursor consumption by secondary electron-stimulated precursor dissociation, precursor arrival, and refresh via the impinging vapor flux and precursor desorption. Supporting Information S18 lists the variables appearing in the equation sequentially with definitions of each provided. This type of EBID model has been used previously in order to understand the steady-state precursor coverage during EBID.[2,9,11,18,19] Here we explored the time-dependent evolution of the nanopillar with the additional caveat of an evolving nanopillar surface morphology. A finite differencing algorithm implementing non-uniform spatial grids was required to account for virtual nanopillar surface evolution.[32] The change in the concentration of dissociated precursor molecules per dwell period $\partial C_d(r,s,t)/\partial t$ was described by

$$\frac{\partial C_d(r,s,t)}{\partial t} = \bar{\sigma}_{30keV}\frac{\partial r}{\partial s}\frac{\delta_{SEI}\left(1 + \sec\left(\tan^{-1}\frac{\partial h(r,t)}{\partial r}\right)\right)i_b}{2\pi q w^2}e^{-r^2/2w^2}C(r,s,t)$$
$$(7)$$

where eq 7 was then converted into the change in nanopillar height using the following expression

$$\partial h(r,t) = \frac{t_{ML}}{d_\rho}\frac{\partial C_d(r,s,t)}{\partial t}\partial t \quad (8)$$

where the term t_{ML}/d_ρ converts a dissociated concentration of precursor molecules into a nanopillar height; t_{ML} is the thickness of a monolayer of deposit, and d_ρ is the surface density of one monolayer of deposit. Precursor dissociation was assumed to occur by SE$_I$ according to the term $\delta_{SEI}(1 + \sec(\tan^{-1}(\partial h(r,t)/\partial r)))i_b$ (see Supporting Information S19), where SE$_I$ emission increases as the nanopillar side wall angle increases. The $\partial r/\partial s$ term coun-

teracts this increase in SE$_I$ emission by accounting for the increase in surface area per radial pixel on the nanopillar sidewalls; $\partial r/\partial s$ is derived from the ratio of the differential areas $\partial A_o/\partial A = (r \times \partial r \times \partial \theta)/(r \times \partial s \times \partial \theta) = \partial r/\partial s$ in the substrate plane (∂A_o) and on the nanopillar surface (∂A), respectively. Rykaczewski et al. constructed a similar comprehensive simulation for the purpose of understanding hydrocarbon dissociation during constant dwell mode ($\tau_r = 0$), focused electron imaging under high vacuum conditions.[20] Their simulation results predict a nanospot profile evolution assuming equilibrium coverage whereby surface diffusion dictates the flow of precursor to the growth spot.[20] Although our EBID growth conditions are far different from those of Rykaczewski et al. (e.g., $\sim 10^3$ difference in precursor pressure), we found qualitative agreement between the growth regime classifications proposed by Rykaczewski et al. and the growth rate profiles anticipated from each regime.[20]

A number of assumptions were made in constructing this model. Anticipated values for the equilibrium precursor coverage were assumed to be $\theta_o \ll 1$, such that a time-independent value of the surface diffusion coefficient could be assumed (this assumption proved to be valid for the system studied, as will be shown in the results presented below). Reversible physisorption of the precursor molecule was assumed as the sole contributor to the modulation of the monolayer-limited surface coverage (nondissociative Langmuir adsorption isotherm).[2] Partial precursor fragmentation almost certainly contributes to the surface coverage based on the fact that highly contaminated deposits are a hallmark of EBID using W(CO)$_6$.[33] However, partial precursor fragmentation is ignored in this work for the purpose of computational tractability. A Gaussian mathematical form was used to describe the incident, focused electron beam spatial profile convolved with the SE$_I$ (secondary electron species of type I) emission profile[18] that primarily stimulates precursor dissociation at the high accelerating voltages of $E_o = 30$ keV;[24] SE$_{II}$ (secondary electron species of type II), BSE (backscattered electron), and FSE (forward scattered electron) induced deposition are negligible for the experiments reported here as described in Supporting Information S19. The maximum surface density of precursor molecules was assumed to be the close-packed arrangement based on the effective molecular diameter of the precursor molecule. A single value for $\bar{\sigma}_{30keV}$ was used in the equation in place of the exact, energy-dependent cross section, which is currently an unknown quantity for the W(CO)$_6$ precursor, although an estimate is available in the literature.[2,27] Thus, $\bar{\sigma}_{30keV}$ represents an average value describing precursor dissociation by an SE$_I$ of average energy. As will be described below, this value was estimated from real EBID experiments and then used in the simulation.

It is widely accepted that SEs both limit the lateral EBID deposit resolution (SE$_{II}$)[1−4,7,34] and represent the dominant contributor to precursor dissociation (SE$_I$ and SE$_{II}$)[15,35−37] as supported by both experiments and simulations. SE-induced dissociation was thus used as the sole cause of precursor dissociation in this work. However, it is noteworthy to mention that dissociation by the incident, primary electron may play a significant role and that simulations have shown that FSEs also contribute to the final deposit volume[17,22,23] for lower voltage settings and taller nanopillar structures relative to the experiments reported here.

Simulation execution proceeded as follows. An initial guess set of (D,τ,δ) was selected from a matrix containing 1760 unique set values. The matrix spanned the following ranges for each parameter $D = 4.8:0.2:6.8$ μm^2 s^{-1}, $\tau = 2.65:0.05:3.60$ ms, and $\delta = 0.0245:0.0005:0.0295$. This refined search range was determined from a much broader sampling of parameter space spanning the ranges $D = 0.1−10$ μm^2 s^{-1}, $\tau = 0.2−4$ ms, and $\delta = 0.01−0.2$. This broad range was sampled in coarse increments. It was found that solutions beyond the course range diverged significantly from experiments based on either θ_o or final nanopillar morphology. The best fit of a parameter set (D,τ,δ) to the experimental data (procedure described below) was taken as the center point for the refined search.

Seven EBID simulations were conducted for each of the 1760 (D,τ,δ) parameter sets replicating each of seven real EBID experiment conducted in a refresh study $\tau_r = 0.50$, 1, 1.5, 2, 4, 6, and

8 ms (Figure 2a). Thus, 12 320 computer simulations were conducted in total amounting to $1^{1/2}$ months of CPU time using an Intel Core2 Quad CPU Q6600 2.40 GHz. Simulated data fits to experimental data were evaluated by minimizing the sum of the squares according to the following expression.

$$\chi^2 = \sum_{\tau_r=0.5\ \text{ms}}^{\tau_r=8\ \text{ms}} (h_f^{\text{sim}} - h_f^{\text{exp}})^2 \qquad (9)$$

where h_f^{sim} and h_f^{exp} are the simulated and experimental values for the final nanopillar height, respectively. The minimum χ^2 value was selected as the best solution for (D,τ,δ). Simulations were then executed by replicating the remainder of the experimental data using this best fit set. This served as an additional test for solution set precision by testing the fitted parameters over a broad range of experimental conditions.

The time evolution of the simulation proceeded as follows. The new precursor surface concentration $C(r,s,t)$ was calculated by discretizing eq 6 over a brief time period Δt. The incident electron flux was either finite or off for the dwell and refresh cycles, respectively. The time period was selected such that the stability criteria $2D\Delta t\Delta x^{-2} < 1$ was met for the forward time central differencing scheme; Δt values on the order of 10^2 ns were required during the beam dwell period for the purpose of computational accuracy. Initial conditions reflecting the real EBID experimental conditions were used where θ_o was established at all points on the substrate surface prior to virtual electron exposure. The change in the nanopillar height $\partial h(r,t)$ was calculated for each simulation time step using eqs 7 and 8. Finally, the precursor concentration was reduced following each dwell time step Δt according to $C_{t+\Delta t} = C_t(A_t/A_{t+\Delta t})$ in order to account for the increase in surface area (A) produced by the formation of a new deposit. This simulation process was repeated sequentially until the number of specified dwell and refresh loops were completed.

The errors in D, τ, and δ are reported in terms of the solution sets that yielded simulation results overlapping the extremes of experimental error owing to the coupled nature of (D,τ,δ) during EBID. These solutions represent the most deviant solutions according to the criteria (1) min(mean($h_f^{\text{exp}} - h_f^{\text{sim}}$)) or max(mean($h_f^{\text{exp}} - h_f^{\text{sim}}$)), which satisfied the additional criteria that (2) 6 of 7 simulated data points had to fall within experimental error.

In addition, error in our parameter set certainly exists from (1) using only estimates of electron and precursor fluxes, (2) ignoring the complex internal structure (spatial variations in composition and phase) observed in real EBID deposits, (3) assuming only a single species (the precursor molecule alone) as rate-limiting precursor adsorption/desorption, (4) ignoring partial precursor fragmentation, and (5) assuming SE$_t$-induced EBID (ignoring FSE and PE induced dissociation) using (6) a mean dissociation cross section as opposed to a full description of $\sigma(E)$, the energy-dependent electron impact precursor dissociation cross section.

Nanopillar Composition. Nanopillar composition fell within the range 15 ± 3 atom % W for the nanopillar features reported in this work (as determined by energy-dispersive X-ray analysis) (see Supporting Information S20). A program was created that calculated values for nanopillar height, volume, width, average density, and surface area using both the nanopillar purity (15 ± 3 atom % W) and an SEM image of the nanopillar profile. Once the composition of the deposit was determined for a deposit grown under RRL conditions, it was possible to determine the number of atoms deposited per electron (γ); γ was converted to an estimate of the mean dissociation cross section using $\bar{\sigma}_{30\text{keV}} = \gamma/(\theta_o \times s_p)$.

REFERENCES AND NOTES

1. Randolph, S.; Fowlkes, J.; Rack, P. D. Focused, Nanoscale Electron-Beam-Induced Deposition and Etching. *Crit. Rev. Solid State Mater. Sci.* **2006**, *31*, 55–89.
2. Utke, I.; Hoffmann, P.; Melngailis, J. Gas-Assisted Focused Electron Beam and Ion Beam Processing and Fabrication. *J. Vac. Sci. Technol., B* **2008**, *26*, 1197–1276.
3. van Dorp, W. F.; Hagen, C. W. a Critical Literature Review of Focused Electron Beam Induced Deposition. *J. Appl. Phys.* **2008**, *104*, 081301-42.
4. van Dorp, W. F.; van Someren, B.; Hagen, C. W.; Kruit, P. Approaching the Resolution Limit of Nanometer-Scale Electron Beam-Induced Deposition. *Nano Lett.* **2005**, *5*, 1303–1307.
5. von Kouwen, L.; Botman, A.; Hagen, C. W.; Kruit, P. Focused Electron-Beam-Induced Deposition of 3 nm Dots in a Scanning Electron Microscope. *Nano Lett.* **2009**, *9*, 2149–2152.
6. van Dorp, W. F.; Lazar, S.; Hagen, C. W.; Kruit, P. Solutions to a Proximity Effect in High Resolution Electron Beam Induced Deposition. *J. Vac. Sci. Technol., B* **2007**, *25*, 1603–1608.
7. van Dorp, W. F.; van Someren, B.; Hagen, C. W.; Kruit, P.; Crozier, P. A. Statistical Variation Analysis of Sub-5-nm-Sized Electron-Beam-Induced Deposits. *J. Vac. Sci. Technol., B* **2006**, *24*, 618–622.
8. Cicoira, F.; Hoffmann, P.; Olsson, C. O. A.; Xanthopoulos, N.; Mathieu, H. J.; Doppelt, P. Auger Electron Spectroscopy Analysis of High Metal Content Micro-Structures Grown by Electron Beam Induced Deposition. *Appl. Surf. Sci.* **2005**, *242*, 107–113.
9. Toth, M.; Lobo, C. J.; Hartigan, G.; Knowles, W. R. Electron Flux Controlled Switching between Electron Beam Induced Etching and Deposition. *J. Appl. Phys.* **2007**, *101*, 054309-6.
10. Randolph, S.; Fowlkes, J. D.; Rack, P. D. Focused Electron-Beam-Induced Etching of Silicon Oxide. *J. Appl. Phys.* **2005**, *98*, 034902.
11. Randolph, S. J.; Fowlkes, J. D.; Rack, P. D. Effects of Heat Generation during Electron-Beam-Induced Deposition of Nanostructures. *J. Appl. Phys.* **2005**, *97*, 124312–124318.
12. Utke, I.; Friedli, V.; Amorosi, S.; Michler, J.; Hoffmann, P. Measurement and Simulation of Impinging Precursor Molecule Distribution in Focused Particle Beam Deposition/Etch Systems. *Microelectron. Eng.* **2006**, *83*, 1499–1502.
13. Friedli, V.; Utke, I. Optimized Molecule Supply from Nozzle-Based Gas Injection Systems for Focused Electron- and Ion-Beam Induced Deposition and Etching: Simulation and Experiment. *J. Phys. D: Appl. Phys.* **2009**, *42*, 125305.
14. Fischer, H.; Wanzenboeck, H. D.; Gottsbachner, J.; Muller, S.; Brezna, W.; Schramboeck, M.; Bertagnolli, E. Direct-Write Deposition with Focused Electron Beam. *Microelectron. Eng.* **2006**, *83*, 784–787.
15. Silvis-Cividjian, N.; Hagen, C. W.; Kruit, P. Spatial Resolution Limits in Electron-Beam-Induced Deposition. *J. Appl. Phys.* **2005**, *98*, 084905.
16. Fowlkes, J. D.; Randolph, S. J.; Rack, P. D. Growth and Simulation of High-Aspect Ratio Nanopillars by Primary and Secondary Electron-Induced Deposition. *J. Vac. Sci. Technol., B* **2005**, *23*, 2825–2832.
17. Smith, D. A.; Fowlkes, J. D.; Rack, P. D. A Nanoscale Three-Dimensional Monte Carlo Simulation of Electron-Beam-Induced Deposition with Gas Dynamics. *Nanotechnology* **2007**, *18*, 265308.
18. Lobo, C. J.; Toth, M.; Wagner, R.; Thiel, B. L.; Lysaght, M. J.

High Resolution Radially Symmetric Nanostructures from Simultaneous Electron Beam Induced Etching and Deposition. *Nanotechnology* **2008**, *19*, 025303.

19. Utke, I.; Friedli, V.; Purrucker, M.; Michler, J. Resolution in Focused Electron- and Ion-Beam Induced Processing. *J. Vac. Sci. Technol., B* **2007**, *25*, 2219–2223.

20. Rykaczewski, K.; White, W. B.; Federov, A. G. Analysis of Electron Beam Induced Deposition (EBID) of Residual Hydrocarbons in Electron Microscopy. *J. Appl. Phys.* **2007**, *101*, 054307.

21. Rack, P., D.; Fowlkes, J., D.; Randolph, S., J. *In Situ* Probing of the Growth and Morphology in Electron-Beam-Induced Deposited Nanostructures. *Nanotechnology* **2007**, *18*, 465602.

22. Smith, D. A.; Fowlkes, J. D.; Rack, P. D. Simulating the Effects of Surface Diffusion on Electron Beam Induced Deposition *via* a Three-Dimensional Monte Carlo Simulation. *Nanotechnology* **2008**, *19*, 415704.

23. Smith, D. A.; Fowlkes, J. D.; Rack, P. D. Understanding the Kinetics and Nanoscale Morphology of Electron-Beam-Induced Deposition *via* a Three-Dimensional Monte Carlo Simulation. *Small* **2008**, *4*, 1382–1389.

24. Joy, D. C. An Introduction to Monte-Carlo Simulations. *Scanning Microsc.* **1991**, *5*, 329–337.

25. Plank, H.; Gspan, C.; Dienstleder, M.; Kothleitner, G.; Hofer, F. The Influence of Beam Defocus on Volume Growth Rates for Electron Beam Induced Platinum Deposition. *Nanotechnology* **2008**, *19*, 485302.

26. Wich, T. , Automated Nanohandling by Microrobots. In *Automated Nanohandling by Microrobots*; Fatikow, S. , Ed.; Springer: London, 2007; pp 295−340.

27. Hoyle, P. C.; Cleaver, J. R. A.; Ahmed, H. Ultralow-Energy Focused Electron Beam Induced Deposition. *Appl. Phys. Lett.* **1994**, *64*, 1448–1450.

28. Petzold, H. C.; Heard, P. J. Ion-Induced Deposition for X-ray Mask Repair Optimization Using a Time-Dependent Model. *J. Vac. Sci. Technol., B* **1991**, *9*, 2664–2669.

29. Amman, M.; Sleight, J. W.; Lombardi, D. R.; Welser, R. E.; Deshpande, M. R.; Reed, M. A.; Guido, L. J. Atomic Force Microscopy Study of Electron Beam Written Contamination Structures. *J. Vac. Sci. Technol., B* **1996**, *14*, 54–62.

30. Kohlmann von Platen, K. T.; Buchmann, L. M.; Petzold, H. C.; Brunger, W. H. In Electron-Beam Induced Tungsten Deposition: Growth Rate Enhancement and Applications in Microelectronics; Proceedings of the 36th International Symposium on Electron, Iron, and Photon Beams, Orlando, FL, 1992; AVS: Orlando, FL, 1992; pp 2690−2694.

31. Bret, T.; Utke, I.; Bachmann, A.; Hoffmann, P. *In Situ* Control of the Focused-Electron-Beam-Induced Deposition Process. *Appl. Phys. Lett.* **2003**, *83*, 4005–4007.

32. Veldman, A. E. P.; Rinzema, K. Playing with Nonuniform Grids. *J. Eng. Math.* **1992**, *26*, 119–130.

33. Porrati, F.; Sachser, R.; Huth, M. The Transient Electrical Conductivity of W-Based Electron-Beam-Induced Deposits during Growth, Irradiation and Exposure to Air. *Nanotechnology* **2009**, *20*, 195301.

34. Silvis-Cividjian, N.; Hagen, C. W.; Leunissen, H. A.; Kruit, P. The Role of Secondary Electrons in Electron-Beam-Induced Deposition Spatial Resolution. *Microelectron. Eng.* **2002**, *61−62*, 693–699.

35. Kohlmann von Platen, K. T.; Chlebek, J.; Weiss, M.; Reimer, K.; Oertel, H.; Brunger, W. H. In Resolution Limits in Electron-Beam Induced Tungsten Deposition; Proceedings of the 16th International Symposium on Electron, Ion, and Photon Beams, San Diego, CA 1993; AVS: San Diego, CA, 1993; pp 2219−2223.

36. Liu, Z. Q.; Mitsuishi, K.; Furuya, K. The Growth Behavior of Self-Standing Tungsten Tips Fabricated by Electron-Beam-Induced Deposition Using 200 keV Electrons. *J. Appl. Phys.* **2004**, *96*, 3983–3986.

37. Tanaka, M.; Shimojo, M.; Han, M.; Mitsuishi, K.; Furuya, K. Ultimate Sized Nano-Dots Formed by Electron Beam-Induced Deposition Using an Ultrahigh Vacuum Transmission Electron Microscope. *Surf. Inter. Anal.* **2005**, *37*, 261–264.